Cell Reports

Report

In Vivo Structures of the *Helicobacter pylori cag* Type IV Secretion System

Graphical Abstract

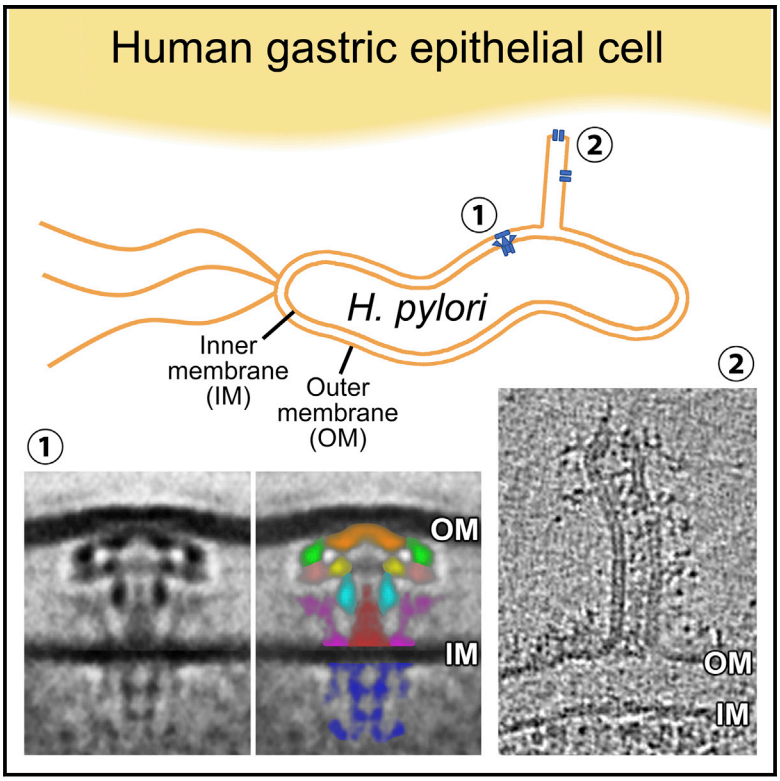

Authors

Yi-Wei Chang, Carrie L. Shaffer, Lee A. Rettberg, Debnath Ghosal, Grant J. Jensen

Correspondence

jensen@caltech.edu

In Brief

Bacteria assemble specialized type IV secretion systems (T4SSs) to inject molecular cargo into target cells. Using electron cryotomography, Chang and Shaffer et al. report the first structure of a cancer-associated T4SS *in vivo* and describe unique membranous appendages that are produced when *H. pylori* encounters gastric epithelial cells.

Highlights

- *H. pylori* assemble unusual tube-like appendages when in proximity to gastric cells
- Architecture of the *cag* T4SS is remarkably similar to that of the *Legionella dot/icm* T4SS
- The *cag* T4SS cytoplasmic apparatus is likely a five-barrel structure

Chang et al., 2018, Cell Reports *23*, 673–681
April 17, 2018
https://doi.org/10.1016/j.celrep.2018.03.085

CellPress

Cell Reports
Report

In Vivo Structures of the *Helicobacter pylori cag* Type IV Secretion System

Yi-Wei Chang,[1,3] Carrie L. Shaffer,[1,3,4] Lee A. Rettberg,[1,2] Debnath Ghosal,[1] and Grant J. Jensen[1,2,5,*]
[1]Division of Biology and Biological Engineering, California Institute of Technology, Pasadena, CA 91125, USA
[2]Howard Hughes Medical Institute, Pasadena, CA 91125, USA
[3]These authors contributed equally
[4]Present address: Department of Veterinary Science, University of Kentucky, Lexington, KY 40546, USA
[5]Lead Contact
*Correspondence: jensen@caltech.edu
https://doi.org/10.1016/j.celrep.2018.03.085

SUMMARY

The type IV secretion system (T4SS) is a versatile nanomachine that translocates diverse effector molecules between microbes and into eukaryotic cells. Here, using electron cryotomography, we reveal the molecular architecture of the *Helicobacter pylori cag* T4SS. Although most components are unique to *H. pylori*, the *cag* T4SS exhibits remarkable architectural similarity to other T4SSs. Our images revealed that, when *H. pylori* encounters host cells, the bacterium elaborates membranous tubes perforated by lateral ports. Sub-tomogram averaging of the *cag* T4SS machinery revealed periplasmic densities associated with the outer membrane, a central stalk, and peripheral wing-like densities. Additionally, we resolved pilus-like rod structures extending from the *cag* T4SS into the inner membrane, as well as densities within the cytoplasmic apparatus corresponding to a short central barrel surrounded by four longer barrels. Collectively, these studies reveal the structure of a dynamic molecular machine that evolved to function in the human gastric niche.

INTRODUCTION

The type IV secretion system (T4SS) is a remarkably versatile molecular machine present in nearly all bacterial phyla and some archaeal species (Christie et al., 2005). Bacteria utilize T4SSs to interact with prokaryotic and eukaryotic cells and to export an incredibly diverse repertoire of substrates (Cascales and Christie, 2003). In most cases, T4SS activity is contact dependent and results in the delivery of nucleoprotein complexes and protein effectors directly into the target cell cytoplasm. By facilitating the exchange of genes and proteins among microbial populations and across kingdoms of life, the T4SS has accelerated bacterial evolution and resulted in species that thrive in diverse environments, including within plant and animal hosts (Christie et al., 2005; Wallden et al., 2010). The gastric bacterium *Helicobacter pylori* exploits the *cag*-pathogenicity-island (*cag*PAI)-encoded T4SS (*cag* T4SS) to translocate a variety of effector molecules into gastric epithelial cells, including the oncoprotein CagA and fragments of peptidoglycan (Fischer, 2011). These translocated effector molecules activate components of the innate immune system and dysregulate signaling pathways that significantly augment the risk of gastric cancer (Amieva and Peek, 2016). When *H. pylori* contacts the gastric cell, the bacterium produces filamentous structures that are dependent on multiple *cag* genes and have been termed *cag* T4SS pili (Barrozo et al., 2013; Jimenez-Soto et al., 2009; Johnson et al., 2014; Kwok et al., 2007; Rohde et al., 2003; Shaffer et al., 2011). While *H. pylori* strains that fail to produce *cag* T4SS pili are unable to translocate cargo to host cells (Johnson et al., 2014; Kwok et al., 2007; Shaffer et al., 2011), the exact role of these filaments in *cag* T4SS activity remains unclear.

The T4SS family is phylogenetically diverse and has been divided into two major sub-types, type IVA and type IVB (T4ASS and T4BSS, respectively). Historically, T4ASSs have been classified according to protein homology to components of *E. coli tra* DNA conjugation systems (types F and P) and the *A. tumefaciens vir* T4SS, while T4BSSs exhibit protein sequence conservation to IncI-like conjugation systems and the *L. pneumophila dot/icm* T4SS (Wallden et al., 2010). In most cases, T4ASSs comprise approximately 12 components with clear homology to Vir proteins, while T4BSSs incorporate many more proteins, and few share sequence homology with *vir* T4SS components (Wallden et al., 2010). The *cag* T4SS has been considered a T4ASS since several Cag proteins share limited sequence similarity to Vir components (Fischer, 2011; Wallden et al., 2010); however, the homologies are so weak that their relevance is unclear, and the *cag*PAI encodes as many genes as a typical T4BSS, including many *H. pylori*-specific genes (Fischer, 2011). In addition, recent work has provided architectural and structural information about several different T4SSs, including the *Escherichia coli* conjugation *tra* T4SS (Fronzes et al., 2009; Low et al., 2014), the *A. tumefaciens vir* T4SS (Gordon et al., 2017), the *Legionella pneumophila dot/icm* T4SS (Ghosal et al., 2017; Kubori et al., 2014), and the *H. pylori cag* T4SS (Frick-Cheng et al., 2016). Among these, the *dot/icm* and *cag* effector translocator systems have many more genes than the *tra* and *vir* DNA-translocating systems, including several

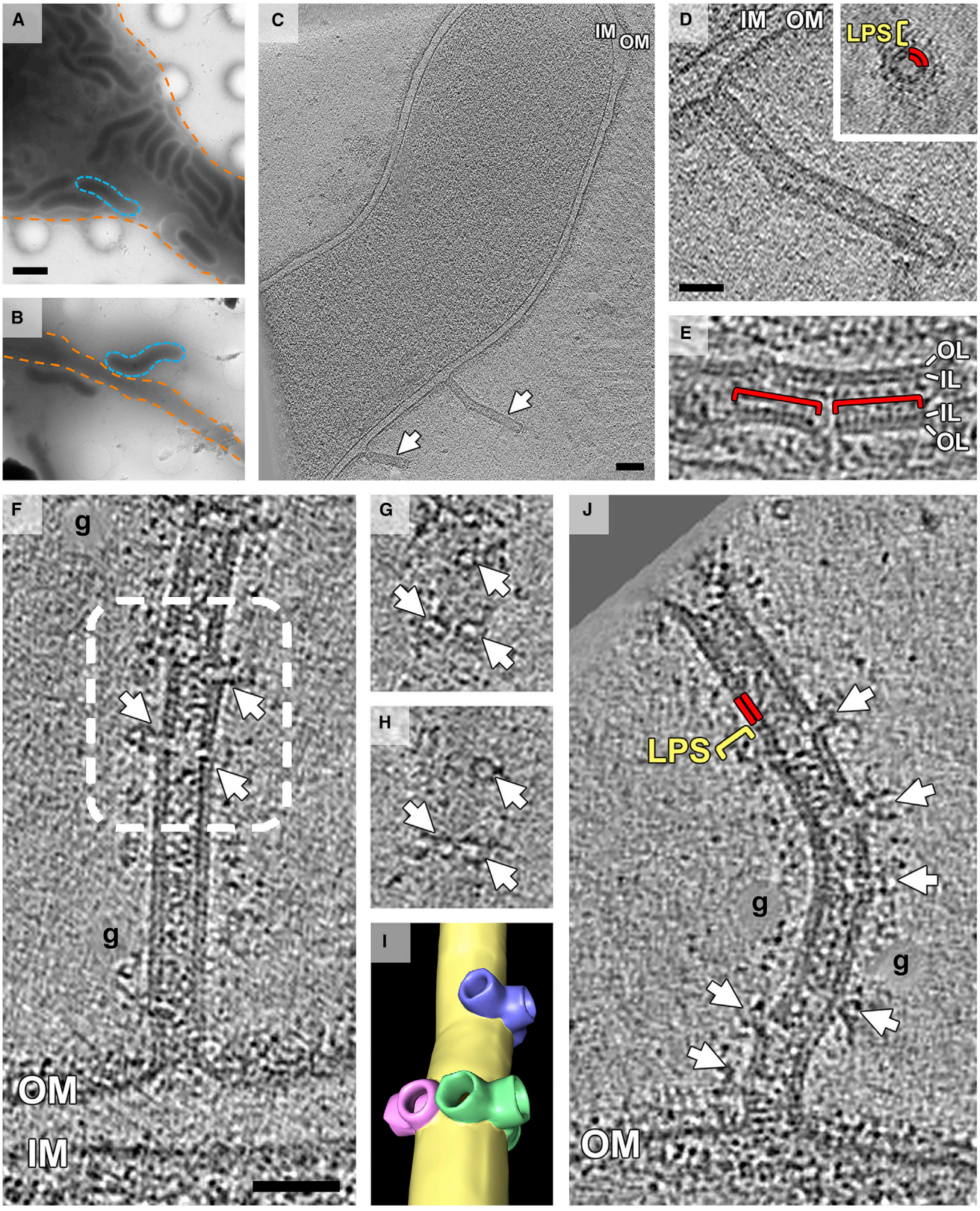

(legend on next page)

without obvious homologs in other bacteria (Frick-Cheng et al., 2016; Ghosal et al., 2017; Kubori et al., 2014). A so-called "core complex" of the *cag* T4SS has been purified and consists of Cag3, CagT, CagM, and two constituents that are orthologous to the VirB9/TraO (CagX) and VirB10/TraF (CagY) subunits of other systems (Fischer, 2011; Frick-Cheng et al., 2016).

In the present study, we applied electron cryotomography (ECT) to image frozen-hydrated *H. pylori* co-cultured with human gastric epithelial cells. We report structures of the intact *cag* T4SS *in vivo* and describe membranous tubes elaborated by *H. pylori* in response to the host cell. Together, these results suggest hypotheses underlying the mechanism of the *cag* T4SS and the roles of its components.

RESULTS

H. pylori Cells Produce Membranous Tube-like Appendages in Response to the Host Cell

Since T4SS activity is stimulated by direct host cell contact, we sought to visualize the *cag* T4SS by imaging *H. pylori* in co-culture with human gastric epithelial cells. In order to avoid interference from flagella or flagellar motors in the analysis, we selected the *cag*PAI-positive, non-flagellated *H. pylori* strain 26695 for our studies. We cultured gastric epithelial cells on electron microscopy grids, infected the grid-adherent monolayers with *H. pylori*, and plunge-froze the co-culture sample to preserve cellular features in a near-native state. We recorded ECT tilt-series of regions of the sample where the bacteria were in direct contact or close proximity to epithelial cell elongations (Figures 1A and 1B). In approximately 5% of the tomograms, we observed striking membranous tubes extending from the outer membrane of wild-type (WT) *H. pylori* cells (Figures 1C and 1D). These tubes were produced only by *H. pylori* that were co-cultured with gastric cells and were not observed in bacteria that were grown in pure culture (n = 464; Figure S1A). While this indicates that the tubes assemble in response to the host cell, we did not observe direct interaction of individual tubes with gastric epithelial cell surfaces (though we cannot rule out the possibility that longer tubes touched host cell surfaces beyond the imaging area of individual tomograms). Densities possibly attributable to lipopolysaccharide (LPS) were clearly visible on the periphery of tube cross-sections, as were both leaflets of the membrane bilayer (Figure 1D, inset). A thin layer of periodic densities lined the interior of the tubes, intimately associated with the inner leaflet of the bilayer, suggesting the presence of a regular protein support scaffold (Figure 1E). The tubes appeared rigid and had membrane outer surface (not including LPS) and inner channel (interior surface of scaffold) diameters of 37 and 22 nm, respectively (Figure S2). Many tubes displayed pipe-like ports (median diameter, 10 nm) along their lengths (Figures 1F–1I). In some cases, ports appeared to induce small bends in the tube (Figure 1J), as if by wedging into the scaffold. The length of individual tubes produced by WT *H. pylori* ranged from 76 to 547 nm, with a median of 193 nm (n = 18; Figure S1B). To our surprise, the tubes were not associated with obvious basal body-like densities localized directly beneath the tube in the periplasm or the inner or outer membranes, suggesting that a dedicated membrane-bound apparatus either is not required for tube formation, not recognizable at the current resolution, or had disassembled prior to sample freezing.

To investigate whether the tubes were related to *cag* T4SS activity, we used ECT to image *H. pylori* lacking either the effector protein CagA, the *cag* T4SS pilus-regulating protein CagH (Shaffer et al., 2011), or the entire *cag*PAI. ECT revealed tubes extending from the bacterial envelope when either *cagA* or *cagH* mutants were co-cultured with gastric cells (Figure S2), but not the *cag*PAI strain. Collectively, tubes were produced by *H. pylori* proximal to a gastric cell in a total of 17 of 336 tomograms of the WT, *cagA*, and *cagH* strains. We visualized roughly equivalent numbers of tubes produced by WT, *cagA*, and *cagH* strains (*cagA*, n = 22; *cagH*, n = 23), and the number of tubes produced per bacterial cell ranged from 1 to 10. Two extremely long tubes (785 nm and 1311 nm) were observed in the *cagH* mutant (Figure S1F), and this strain also assembled a few tubes with larger outer and inner diameter dimensions (Figure S1).

In Vivo Ultrastructure of the *cag* T4SS

In some tomograms, we noticed dense, periplasmic, cone-shaped particles spanning the bacterial envelope near membrane tubes (Figures 2A and 2B). These structures were reminiscent of *L. pneumophila dot/icm* T4SS complexes observed *in situ* (Ghosal et al., 2017) and consisted of distinct layers of densities in the periplasmic space near the outer membrane (Figure 2B). Based on the structural similarity to the *dot/icm* T4SS,

Figure 1. *H. pylori* Assembles Membranous Tubes When Proximal to Gastric Epithelial Cells

(A) Low-magnification view of a gastric epithelial cell grown on an electron microscopy grid and infected with *H. pylori*.

(B) Low-magnification view of *H. pylori* interacting with a gastric epithelial cell surface. In (A) and (B), blue dashed lines indicate examples of *H. pylori* that were imaged by ECT, and orange dashed lines demarcate the edges of individual gastric epithelial cells.

(C) Tomographic slice through WT *H. pylori* co-cultured with gastric epithelial cells. Arrows indicate membrane tubes extending from the *H. pylori* cell envelope.

(D) Enlarged view of the longer tube shown in (C). Inset: cross-section of a membrane tube. The two leaflets of the tube membrane bilayer are labeled by two red lines; LPS is indicated by a yellow bracket.

(E) Periodic densities lining the inside of the tube (red brackets).

(F) An individual tube displaying lateral ports (arrows).

(G and H) Distal (G) and proximal (H) cross-sections of ports within the boxed region of the tube depicted in (F).

(I) 3D segmentation of the boxed region in (F).

(J) Lateral ports (arrows) appeared to induce a slight bending of the tube. The two leaflets of the tube and lipopolysaccharide densities decorating the surface are labeled as in (D). The locations of erased gold fiducials during tomogram reconstruction are labeled with "g."

Scale bars: 2 μm in (A), which applies to (A) and (B); 100 nm in (C); 50 nm in (D); 50 nm in (F), which applies to (E)–(H) and (J). OM, outer membrane; IM, inner membrane; OL, outer leaflet; IL, inner leaflet.

See also Figure S1.

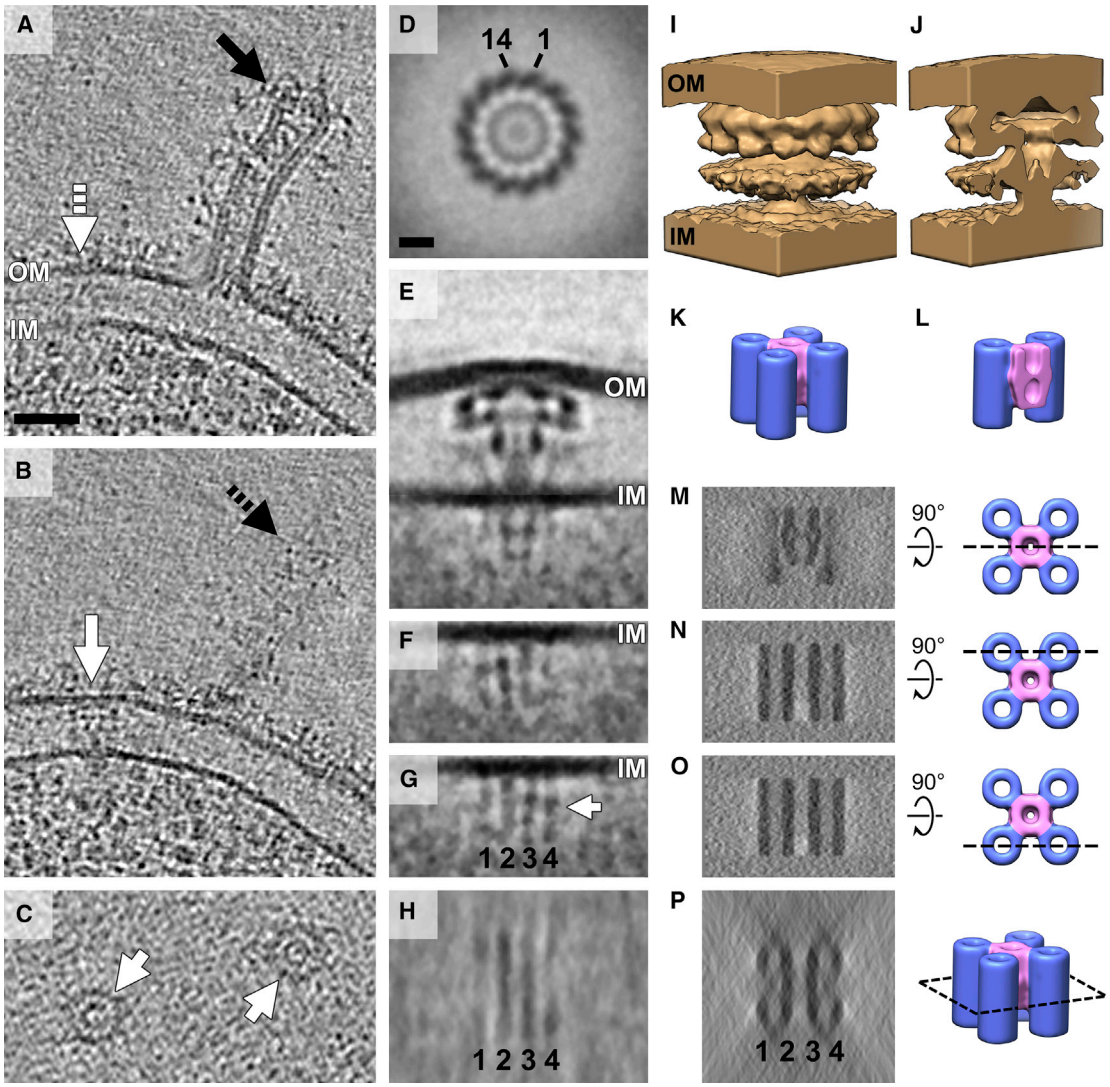

Figure 2. *In Vivo* Structure of the *cag* T4SS

(A and B) Distal (A) and proximal (B) tomographic slices of the same region of the bacterial envelope identifying a *cag* T4SS particle (white arrow) adjacent to a tube-like appendage (black arrow). Dashed arrows represent the position of the tube and *cag* T4SS particle in the other tomographic slice.

(C) Top views of individual *cag* T4SS particles (arrows).

(D) Top view of the sub-tomogram average of *cag* T4SS reveals 14-fold symmetry. Numbers indicate the clockwise count of individual subunits visible in the ring structure.

(E) Central slice through the side view of the composite sub-tomogram average of the *cag* T4SS. Averages aligned on the periplasmic and cytoplasmic parts are stitched using the IM as the boundary.

(F and G) Distal (F) and proximal (G) off-center tomographic slices of the cytoplasmic apparatus from the side view reveal four distinct rod-like densities.

(H) A top view of the cytoplasmic apparatus at the level of the white arrow in (G) shows two central lines and four corner densities.

(I and J) 3D representation (I) and cut-away view (J) of the *cag* T4SS periplasmic structure.

(K and L) 3D representation (K) and cut-away view (L) of the predicted five-barrel structure of the cytoplasmic apparatus. The shorter central barrel is indicated in light pink.

(M–P) Simulated tomograms of the five-barrel model of the cytoplasmic apparatus corresponding to tomographic slices E (M), F (N), G (O), and H (P). The position of each predicted tomographic slice is indicated in the views of the five-barrel model to the right.

Scale bars: 50 nm in (A), which applies to (A)–(C); 10 nm in (D), which applies to (D)–(H). OM, outer membrane; IM, inner membrane.

See also Figure S2.

we hypothesized that these structures corresponded to a T4SS. Close inspection of our tomograms revealed varying numbers of these particles in each *H. pylori* cell (ranging from 0 to 4 particles per cell in the field of view of the tomograms). The particles were found at cell poles and lateral cell surfaces, consistent with previous reports analyzing *cag* T4SS components (Barrozo et al.,

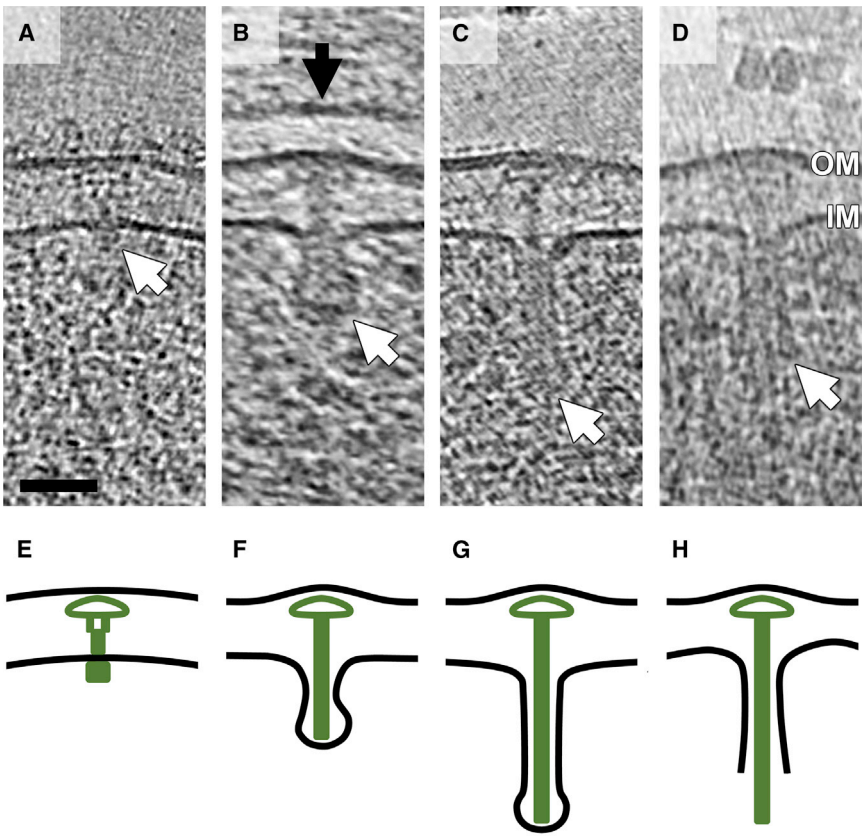

Figure 3. Pilus-like Rods Emerging from the *cag* T4SS

(A) *cag* T4SS particle exhibiting a typical cytoplasmic structure (arrow).

(B) *cag* T4SS particle with a pilus-like rod density surrounded by an IM invagination (white arrow). The gastric epithelial cell plasma membrane (black arrow) is visible directly above the bacterial outer membrane.

(C) *cag* T4SS particle with an extended pilus-like rod density and IM sheath (arrow).

(D) *cag* T4SS particle with a long pilus-like rod density that appears to have ruptured the IM (arrow).

(E–H) Schematic interpretation of the *cag* T4SS apparatus conformation in (A) (shown in E), (B) (shown in F), (C) (shown in G), and (D) (shown in H). Scale bar: 50 nm in (A), which applies to (A)–(D). OM, outer membrane; IM, inner membrane.

2013; Kwok et al., 2007; Rohde et al., 2003; Shaffer et al., 2011). In many instances, we observed the bacterial outer membrane bulging to accommodate the assembled particle. We also captured several top views of the structure, which revealed two concentric rings. The outer ring exhibited 14-fold symmetry (Figures S2A, S2B, and S2D) and a diameter of 40 nm (Figures 2C and 2D), consistent with the structure of immunopurified *cag* T4SS core complexes resolved by negative-stain electron microscopy (Frick-Cheng et al., 2016). Among the four potential T4SSs harbored by *H. pylori*, the imaged strain lacks complete *tfs3* and *tfs4* systems, and although the strain harbors the *comB* T4SS, corresponding cone-shaped particles were never observed in over 100 tomograms of the cognate *cag*PAI mutant strain co-cultured with gastric epithelial cells, leading us to conclude that these particles are the *cag* T4SSs rather than the *comB* DNA uptake or other T4SSs.

To investigate structural details of the *cag* T4SS, we sought to generate a sub-tomogram average. Given the inherent structural flexibility of other T4SSs (Ghosal et al., 2017; Low et al., 2014), we aligned and averaged the periplasmic and cytoplasmic regions separately and then generated a composite average (Figure 2E). In total, 67 *cag* T4SS particles were captured and used to generate the average. Determined through Fourier shell correlation, the final resolutions of the periplasmic and cytoplasmic parts were 3.9 nm and 6.8 nm, respectively (Figures S2C and S2D). In the periplasm, we resolved a "hat" density associated with the outer membrane, several ring-like densities surrounding and beneath the hat, a central stalk, and wing-like densities on the periphery (Figures 2E, 2I, and 2J). Cross-sections through the cytoplasmic apparatus revealed parallel lines of density (Figures 2E–2H), but because most of the *cag* T4SS particles used in the average were imaged from the side (electron beam parallel to the membranes), the average was smeared by the missing wedge effect in that direction. Therefore, to interpret these densities, we explored a variety of candidate structures by generating artificial tomograms smeared by the same missing wedge effect and then compared their cross-sections to the experimental data (Figures S2E–S2H). We tested configurations of one to six barrel densities and various combinations of barrel and rod structures. The best matching model consisted of a short central barrel surrounded by four longer barrels, which together recapitulated the experimental results (Figures 2E–2H, 2K–2P; Figure S2).

Sheathed Cytoplasmic Rod within the *cag* T4SS

In three unusual *cag* T4SS particles (out of a total of 70 particles), we observed a dense, central rod extending from the outer-membrane-associated complex into inner membrane invaginations with different depths (Figures 3B–3D and 3F–3H). This feature was not observed previously in the *dot/icm* T4SS or in the purified R388 T4SS particles (Ghosal et al., 2017; Low et al., 2014). The rod and inner membrane invaginations measured ~10 nm and 30 nm in width, respectively, and the rod extended 45–120 nm from the outer membrane complex (Figures 3B–3D). Notably, in one of the particles, the rod appeared to project through the inner membrane into the cytoplasm, though the details of this event were obscured by the crowded cytoplasm (Figures 3D and 3H).

Comparison to Previous T4SS Structures

To explore the structural relationships between T4SSs, we compared the *cag* T4SS sub-tomogram average to the previous

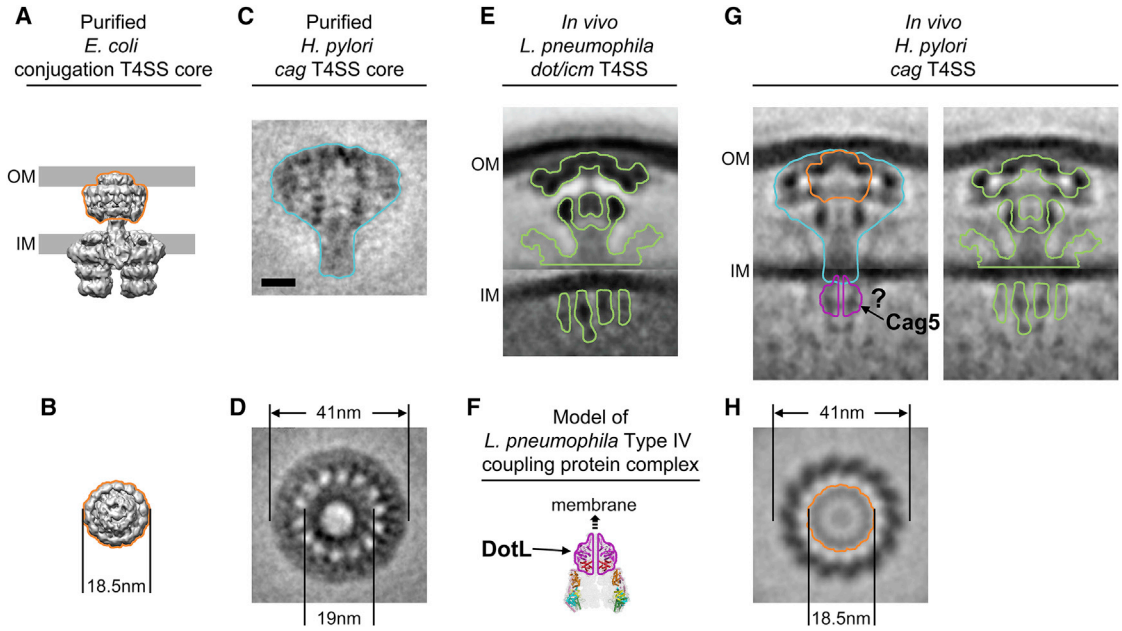

Figure 4. Comparison of Diverse T4SS Machinery Structures

(A and B) Side (A) and top (B) views of the purified *E. coli* R388 conjugation system (Low et al., 2014).

(C and D) Side (C) and top (D) views of immunopurified *cag* T4SS core complex particles (adapted and modified from Frick-Cheng et al. [2016]).

(E) Side view of the *L. pneumophila dot/icm* T4SS *in vivo* (Ghosal et al., 2017).

(F) Model of the *L. pneumophila* DotL coupling protein complex (Kwak et al., 2017), with the DotL structure outlined in magenta.

(G and H) Side (G) and top (H) views of the *cag* T4SS structure *in vivo* (present study). In (G), two duplicated side views are shown for clearer labeling. Orange outline indicates comparison of the R388 core complex to the *cag* T4SS structure; blue outline indicates the position of the purified *cag* T4SS core complex within the *in vivo* structure; magenta outline indicates the predicted location of the coupling protein Cag5 based on the structure of the DotL homolog shown in (F); green outline indicates the *L. pneumophila dot/icm* T4SS structure superimposed on the *cag* T4SS structure.

Scale bar: 10 nm in (C), which applies to all panels.

See also Figures S3 and S4.

electron microscopy (EM) structures of purified sub-complexes of the R388 (Low et al., 2014) (Figures 4A and 4B), negatively stained sub-complexes of the *cag* T4SS (Figures 4C and 4D), and the sub-tomogram average of the *in vivo dot/icm* T4SS (Ghosal et al., 2017) (Figure 4E; Figure S3). In comparison to the R388 structures, the *cag* T4SS is similar in that it includes a large cluster of densities associated with the outer membrane, a stalk that connects the outer-membrane-associated cap to the inner membrane, and structures in the cytoplasm anchored to the inner membrane (Figures 4A and 4G). The size and shape of the R388 outer-membrane-associated cluster (referred to in Fronzes et al. [2009] as the "core complex" containing the C termini of VirB7, VirB9, and VirB10) matched the hat and inner ring density (labeled δ in Figure S3E) in the *cag* T4SS structure (Figures 4A, 4B, 4G, and 4H, orange demarcation). Because the CagY C terminus shares homology with VirB10 (Fischer, 2011; Rohde et al., 2003) and CagX shares homology with VirB9 (Fischer, 2011; Tanaka et al., 2003), we reason that CagX and CagY form the hat and the density labeled δ. The size of the stalk and the configuration of the cytoplasmic barrels in the two structures, however, appear to be quite different.

In comparison to the images of the purified *cag* T4SS sub-complex that comprise CagM, CagT, CagX/VirB9, CagY/VirB10, and Cag3 (Figures 4C and 4G, blue demarcation), the periplasmic portion of the *in vivo cag* T4SS average exhibited almost the exact size and general shape, which allowed us to definitively position and orient the negative-stain result relative to the bacterial envelope. Comparison of the particle top views also revealed striking structural similarities, including in the sizes of the concentric rings and their 14-fold symmetry (Figures 4D and 4H). These observations further confirm that the particles averaged in this study are the *cag* T4SSs. From this comparison, and based on previous experimental evidence (Frick-Cheng et al., 2016), we conclude that CagT, Cag3, and CagM must produce the densities inside the blue outline but outside the orange in Figure 4G (which were already assigned to CagX/VirB9 and CagY/VirB10). CagT and Cag3 can be further pinpointed as the upper and lower outer rings (α and β in Figure S3E) based on the published negative-stain images of the CagX, CagY, and CagM sub-complex (Frick-Cheng et al., 2016), which are missing those rings (though which form the upper and the lower rings or, if they are mixed, remain unclear). By elimination, this suggests that CagM produces the density labeled γ in Figure S3E; however, CagM localization could be more complicated and so remains to be verified.

Compared to the *in vivo dot/icm* T4SS structure, the *cag* T4SS structure is remarkably similar, considering the fact that the systems each comprise over 25 components and only a few share

sequence homology (Figure S3G). Both structures exhibit (1) an outer-membrane associated hat; (2) upper and lower outer ring-like densities surrounding the hat (labeled α and β in Figures S3E and S3F); (3) a barrel-like γ density at the center of the structure; (4) a central stalk; (5) weak, wing-like densities that extend from the inner membrane into the periplasm, and (6) parallel elongated densities perpendicular to the membrane in the cytoplasm (Figures S3C–S3F). While the upper and outer ring densities (α) superimpose well (Figure 4G, right panel), a difference is that there are two densities in the lower ring of the *cag* T4SS (labeled β and δ in Figure S3E) versus only one (labeled β in Figure S3F) in the *dot/icm* T4SS. Based on a recent report describing the structure of the *L. pneumophila dot/icm* coupling protein DotL (Kwak et al., 2017), its predicted position within the secretion system just underneath the inner membrane (IM) (Kwak et al., 2017), and its match in size and shape to the central barrel seen at the same location in the *H. pylori* sub-tomogram average, we speculate that the central barrel of the cag T4SS cytoplasmic density corresponds to the Cag5/VirD4 coupling protein (Figures 4F and 4G, magenta demarcation; Figure S3H). The tentative positioning of Cag5 to the central barrel density of the cytoplasmic apparatus is further supported by recent work demonstrating that the VirD4 coupling protein is situated in the center of the R388 IM complex between VirB4 barrels (Redzej et al., 2017). Future work imaging deletion mutants will be needed to confirm or refute this speculation. Collectively, these data reveal that, although the cag T4SS is phylogenetically distinct from both the R388 and the *dot/icm* T4SS, the architecture of these three T4SS machines is remarkably conserved.

DISCUSSION

Here, we have reported the structure of the *cag* T4SS and shown that, when *H. pylori* are in proximity to host cells, the bacterium produces membranous tubes decorated with pipe-like ports. Multiple scanning electron microscopy (SEM) studies have shown that, under similar conditions, *H. pylori* assembles extracellular filaments (Jimenez-Soto et al., 2009; Johnson et al., 2014; Kwok et al., 2007; Rohde et al., 2003; Shaffer et al., 2011). In previous papers, these structures have been referred to as "pili," "*cag* T4SS-associated pili," "filaments," "extensions," etc., but here we will refer to all of the previously observed structures as "SEM filaments" for clarity, also because we would like to use the word "pilus" for a single component of the structure (the rod) described later. We propose that the membrane tubes visualized by ECT are the native form of the previously described SEM filaments for the following reasons. First, both the membrane tubes and SEM filaments were only observed when *H. pylori* was co-cultured with gastric epithelial cells. Second, in all cases, both structures depended on the presence of the genes in the *cag*PAI. Third, one previous study interpreted the SEM filaments as proteinaceous pili covered by membrane sheaths (Rohde et al., 2003). Fourth, and most decisively, deletion of the CagH "molecular ruler" protein resulted in both longer and wider membrane tubes and longer and wider SEM filaments (Shaffer et al., 2011). Concerning size, unfortunately, the different SEM studies reported substantially different diameters for the SEM filaments, ranging from 15 to 70 nm (Barrozo et al., 2013; Johnson et al., 2014; Kwok et al., 2007; Rohde et al., 2003; Shaffer et al., 2011). While this range does include the diameter of the native membrane tubes measured here, we speculate that, in the previous SEM studies, the extensive chemical fixation, dehydration, and metal coating inherent to the method may have introduced the variations.

Previous SEM immunolabeling experiments showed that CagY is present along the SEM filaments (Jimenez-Soto et al., 2009; Rohde et al., 2003) and that CagT is clustered in ring-like formations at the SEM filament base (Rohde et al., 2003). Other studies showed that additional Cag proteins could be localized to the SEM filaments, including CagA, CagL, CagT, and CagX (Barrozo et al., 2013; Jimenez-Soto et al., 2009; Kwok et al., 2007; Rohde et al., 2003; Tanaka et al., 2003). Because both the *cag* T4SS core complex and SEM filaments/membrane tubes have been associated with CagY, CagT, and CagX, we propose that the *cag* T4SS and the tubes are different states of the same secretion apparatus. In support of this, we note that the outer and inner diameters of the membrane tubes (37 and 22 nm, respectively) approximately match the outer and inner ring dimensions of the *cag* T4SS (41 and 19 nm, respectively). Alternatively, the membrane tubes may be a different part or assembly of the *cag* T4SS.

More specifically, we propose as a working hypothesis that the T4SS structure shown here (Figure 2E) is a "pre-extension" state that assembles in response to the presence of a host cell (Figure S4A). It is known that the *E. coli tra* and *A. tumefaciens vir* T4SSs produce protein pili. In the *tra* system, the protein F pilus has an outer diameter of 8.7 nm and is formed by the major pilin TraA/VirB2, which is otherwise found in the IM (Costa et al., 2016). Our data reveal that the *cag* T4SS also produces a rod-like structure with a similar diameter in the periplasm (Figure 3). Therefore, we propose that the *cag* T4SS also assembles a protein pilus (the rod) from subunits in the IM (Figures S4B and S4C). This pilus may be formed of CagC, which exhibits weak homology with the VirB2/TraA component in the *vir* T4SS (Andrzejewska et al., 2006; Johnson et al., 2014). In our working model, we propose that, as the pilus grows upward from the IM, it interacts with components of the core complex within the periplasm, possibly opening a translocation channel through the system (Christie et al., 2005). At the onset of membrane tube formation, a conformational change within the core complex disengages the CagX/CagY hat, which is released from the CagT/Cag3 outer ring, and extended tubes are produced by growth of the thin protein scaffold lining the inside tube surface (Figure S4C). The tubes could be stabilized by the CagT/Cag3 outer ring, which remains at the base like a collar, and the scaffold, which holds their diameter constant along their length. This scaffold may contain the VirB5-like CagL (Kwok et al., 2007; Shaffer et al., 2011). If some part of CagL extended through the outer leaflet of the tube lipid bilayer, it would explain the observations that CagL can bind host cell integrins and can be localized to the SEM filaments by immunogold labeling (Kwok et al., 2007). CagI, which can also bind integrins (Jimenez-Soto et al., 2009), may also be part of the scaffold (Pham et al., 2012; Shaffer et al., 2011). This model would explain why CagL and CagI deletion mutants have no SEM filaments (Shaffer et al., 2011). Given that CagH is membrane bound, plays an essential role in T4SS activity,

regulates SEM filament/tube dimensions, and forms a complex with CagL and CagI (Shaffer et al., 2011), CagH may control the incorporation of CagI and CagL into the scaffold (Pham et al., 2012; Shaffer et al., 2011).

We propose that the CagX/CagY hat is a membrane-fusion machine positioned within the tubes. We propose that, upon contact with a host cell, CagX/CagY fuses the tube and host membranes, opening a channel for the passage of effectors (Figure S4D). Our interpretation of the tube ports is that they are open CagX/CagY channels, and this may explain the immunolabeling results that CagY can be localized along the length of the SEM filaments (Jimenez-Soto et al., 2009; Rohde et al., 2003), as well as the observation that the C-terminal/VirB10 domain region of CagY can bind host integrins (Jimenez-Soto et al., 2009). While one CagX/CagY complex may be positioned at the tip of the tube, other complexes present in the outer membrane (OM) may be drawn upward into the tube as it extends, or, alternatively, additional CagX/CagY complexes may assemble in the tubes' lateral walls after extension. The interpretation that CagY is the membrane-fusion protein could explain why strains lacking *cagY* form SEM filaments but do not secrete effector molecules (Barrozo et al., 2013; Johnson et al., 2014), and it is consistent with the proposal that CagY serves as a molecular switch that regulates secretion activity *in vivo* (Barrozo et al., 2013). In the imaged strains, the lateral ports exhibited a diameter of ~10–12 nm, which is large enough to facilitate transport of the folded CagA effector protein, whose dimensions measure 8 × 11 × 5.5 nm (Hayashi et al., 2012). One problem with this model is what happens to the IM transmembrane domain of CagY; given its tether to the IM, how would it remain at the tip of the extending tube? One possibility is that, as the IM is perturbed by pilin subunits being loaded out of the IM and onto the base of the pilus, and as the pilus itself may incorporate IM lipids similar to *E. coli tra* F pili (Costa et al., 2016), the CagY tether is somehow released. Another possibility is that, as CagY is ~1,900 amino acids long, it spans the length of the tube.

Our interpretation of the three unusual T4SS particles with pili protruding downward toward the cytoplasm (Figure 3) is that these are stalled end states in which the CagX/CagY hat failed to disengage the CagT/Cag3 ring, forcing pilus growth to push the IM downward instead of the outer membrane upward. It may, therefore, be that the only states captured in cryotomograms are long lived, including the pre-extension state (Figure S4A), various stalled "failure-to-fire" states (Figure S4C'), and terminal end states of tubes no longer connected to the host, leaving the tubes to reseal at the tip (Figure S4E). Future studies will focus on earlier stages of the association and on bacteria directly touching host cells, in hopes of producing images of the hypothesized transitory states (Figures S4B–S4D).

The role and fate of the pilus itself remains particularly unclear. While pilus growth might be involved in tube extension, a recent study revealed that SEM filaments can be produced by a strain lacking *cagC* (Johnson et al., 2014), and it is also known that strains lacking *cagC* do not secrete *cag* T4SS effectors (Andrzejewska et al., 2006; Johnson et al., 2014). Perhaps there is some required interaction between the putative CagC pilus and the core complex that primes the machinery for effector translocation. Alternatively, as proposed for VirB2 in other type IVA systems (Christie et al., 2005), CagC may form a stable, rod-like translocation channel or pore through the periplasmic core complex into the base of the tube when the system is actively secreting effector molecules. We emphasize that these speculations are simply our current working hypotheses, and much further work will be needed to confirm or refute this model.

Assuming our model is correct, the *H. pylori cag* T4SS differs from the *E. coli tra* or *A. tumefaciens vir* systems in that the *cag* T4SS produces an extracellular appendage enclosed by outer membrane. Perhaps all T4SSs will share the basic central machinery that loads a VirB9/VirB10 membrane-fusion machine at the tip of an appendage (pilus or tube) that then extends to open a channel into a host cell, but perhaps they will also differ in the presence and roles of peripheral proteins that manage the outer membrane involvement in that appendage. Functionally, exposed protein pilus may, alone, be sufficient to translocate single-stranded DNA (Shu et al., 2008), but wide membrane tubes like those seen here may be required to translocate folded effector proteins into a host. Interestingly, some authors have proposed that membrane tubes are involved in DNA translocation (Anderson, 1958; Anderson et al., 1957).

EXPERIMENTAL PROCEDURES

Bacterial Strains and Growth Conditions

H. pylori strain 26695 and corresponding mutants (Shaffer et al., 2011) were routinely maintained on Trypticase soy agar supplemented with 5% sheep blood (BD Biosciences) under microaerobic conditions. For all experiments, *H. pylori* cells were seeded into Brucella broth supplemented with 10% fetal bovine serum (FBS) and were grown overnight in shaking culture at 37°C, 5% CO_2. Overnight bacterial cultures were normalized to an optical density at 600 nm (OD_{600}) to ~0.3 in fresh Brucella broth supplemented with 10% FBS, and cells were grown to mid-log phase at 37°C, 5% CO_2, prior to generating samples for microscopy analysis.

Human Cell Culture

The gastric adenocarcinoma cell line AGS (ATCC CRL-1739) was maintained in RPMI 1640 medium supplemented with 10% FBS, 2 mM L-glutamine, and 10 mM HEPES buffer. Cells were grown at 37°C in 5% CO_2.

Electron Cryotomography

Detailed methods of electron cryotomography sample preparation, data collection, and data processing are outlined in the Supplemental Experimental Procedures.

Statistical Analysis

The statistical analysis was undertaken in GraphPad Prism 7 by one-way ANOVA, followed by Dunnett's multiple comparisons test.

DATA AND SOFTWARE AVAILABILITY

The accession numbers for the sub-tomogram averages of *cag* T4SS machinery that support the findings of this study are EMDB: 7474 (aligned on the periplasmic region) and EMDB: 7475 (aligned on the cytoplasmic region).

SUPPLEMENTAL INFORMATION

Supplemental Information includes Supplemental Experimental Procedures and four figures and can be found with this article online at https://doi.org/10.1016/j.celrep.2018.03.085.

ACKNOWLEDGMENTS

We thank Dr. Tim Cover for providing *H. pylori* strains and Dr. Joseph Vogel and Dr. Maria Hadjifrangiskou for helpful discussions. This work was supported by NIH grant R01 AI127401 to G.J.J., NIH grant F32 DK105720 to C.L.S., NIH grant T32 A1007474 to C.L.S., and the Burroughs Wellcome Fund 2016 Collaborative Research Travel Grant 1016383 to C.L.S.

AUTHOR CONTRIBUTIONS

Y.-W.C., C.L.S., and L.A.R. prepared the samples. Y.-W.C. collected and processed the electron cryotomography data and generated the sub-tomogram averages. All authors analyzed and interpreted the electron cryotomography data. G.J.J. supervised the project. Y.-W.C., C.L.S., and G.J.J. wrote the paper, with input from all authors.

DECLARATION OF INTERESTS

The authors declare no competing interests.

Received: October 16, 2017
Revised: January 16, 2018
Accepted: March 19, 2018
Published: April 17, 2018

REFERENCES

Amieva, M., and Peek, R.M. (2016). Pathobiology of *Helicobacter pylori*-induced gastric cancer. Gastroenterology *150*, 64–78.

Anderson, T.F. (1958). Recombination and segregation in *Escherichia coli*. Cold Spring Harb. Symp. Quant. Biol. *23*, 47–58.

Anderson, T.F., Wollman, E.L., and Jacob, F. (1957). Ann. Inst. Pasteur (Paris) *93*, 450–455.

Andrzejewska, J., Lee, S.K., Olbermann, P., Lotzing, N., Katzowitsch, E., Linz, B., Achtman, M., Kado, C.I., Suerbaum, S., and Josenhans, C. (2006). Characterization of the pilin ortholog of the *Helicobacter pylori* type IV *cag* pathogenicity apparatus, a surface-associated protein expressed during infection. J. Bacteriol. *188*, 5865–5877.

Barrozo, R.M., Cooke, C.L., Hansen, L.M., Lam, A.M., Gaddy, J.A., Johnson, E.M., Cariaga, T.A., Suarez, G., Peek, R.M., Jr., Cover, T.L., et al. (2013). Functional plasticity in the type IV secretion system of *Helicobacter pylori*. PLoS Pathog. *9*, e1003189.

Cascales, E., and Christie, P.J. (2003). The versatile bacterial type IV secretion systems. Nat. Rev. Microbiol. *1*, 137–149.

Christie, P.J., Atmakuri, K., Krishnamoorthy, V., Jakubowski, S., and Cascales, E. (2005). Biogenesis, architecture, and function of bacterial type IV secretion systems. Annu. Rev. Microbiol. *59*, 451–485.

Costa, T.R., Ilangovan, A., Ukleja, M., Redzej, A., Santini, J.M., Smith, T.K., Egelman, E.H., and Waksman, G. (2016). Structure of the bacterial sex F pilus reveals an assembly of a stoichiometric protein-phospholipid complex. Cell *166*, 1436–1444.e10.

Fischer, W. (2011). Assembly and molecular mode of action of the *Helicobacter pylori* Cag type IV secretion apparatus. FEBS J. *278*, 1203–1212.

Frick-Cheng, A.E., Pyburn, T.M., Voss, B.J., McDonald, W.H., Ohi, M.D., and Cover, T.L. (2016). Molecular and structural analysis of the *Helicobacter pylori cag* type IV secretion system core complex. MBio *7*, e02001–e02015.

Fronzes, R., Schafer, E., Wang, L., Saibil, H.R., Orlova, E.V., and Waksman, G. (2009). Structure of a type IV secretion system core complex. Science *323*, 266–268.

Ghosal, D., Chang, Y.W., Jeong, K.C., Vogel, J.P., and Jensen, G.J. (2017). *In situ* structure of the *Legionella* Dot/Icm type IV secretion system by electron cryotomography. EMBO Rep. *18*, 726–732.

Gordon, J.E., Costa, T.R.D., Patel, R.S., Gonzalez-Rivera, C., Sarkar, M.K., Orlova, E.V., Waksman, G., and Christie, P.J. (2017). Use of chimeric type IV secretion systems to define contributions of outer membrane subassemblies for contact-dependent translocation. Mol. Microbiol. *105*, 273–293.

Hayashi, T., Senda, M., Morohashi, H., Higashi, H., Horio, M., Kashiba, Y., Nagase, L., Sasaya, D., Shimizu, T., Venugopalan, N., et al. (2012). Tertiary structure-function analysis reveals the pathogenic signaling potentiation mechanism of *Helicobacter pylori* oncogenic effector CagA. Cell Host Microbe *12*, 20–33.

Jimenez-Soto, L.F., Kutter, S., Sewald, X., Ertl, C., Weiss, E., Kapp, U., Rohde, M., Pirch, T., Jung, K., Retta, S.F., et al. (2009). *Helicobacter pylori* type IV secretion apparatus exploits beta1 integrin in a novel RGD-independent manner. PLoS Pathog. *5*, e1000684.

Johnson, E.M., Gaddy, J.A., Voss, B.J., Hennig, E.E., and Cover, T.L. (2014). Genes required for assembly of pili associated with the *Helicobacter pylori cag* type IV secretion system. Infect. Immun. *82*, 3457–3470.

Kubori, T., Koike, M., Bui, X.T., Higaki, S., Aizawa, S., and Nagai, H. (2014). Native structure of a type IV secretion system core complex essential for *Legionella* pathogenesis. Proc. Natl. Acad. Sci. USA *111*, 11804–11809.

Kwak, M.J., Kim, J.D., Kim, H., Kim, C., Bowman, J.W., Kim, S., Joo, K., Lee, J., Jin, K.S., Kim, Y.G., et al. (2017). Architecture of the type IV coupling protein complex of *Legionella pneumophila*. Nat. Microbiol. *2*, 17114.

Kwok, T., Zabler, D., Urman, S., Rohde, M., Hartig, R., Wessler, S., Misselwitz, R., Berger, J., Sewald, N., Konig, W., et al. (2007). *Helicobacter* exploits integrin for type IV secretion and kinase activation. Nature *449*, 862–866.

Low, H.H., Gubellini, F., Rivera-Calzada, A., Braun, N., Connery, S., Dujeancourt, A., Lu, F., Redzej, A., Fronzes, R., Orlova, E.V., et al. (2014). Structure of a type IV secretion system. Nature *508*, 550–553.

Pham, K.T., Weiss, E., Jimenez Soto, L.F., Breithaupt, U., Haas, R., and Fischer, W. (2012). CagI is an essential component of the *Helicobacter pylori* Cag type IV secretion system and forms a complex with CagL. PLoS ONE *7*, e35341.

Redzej, A., Ukleja, M., Connery, S., Trokter, M., Felisberto-Rodrigues, C., Cryar, A., Thalassinos, K., Hayward, R.D., Orlova, E.V., and Waksman, G. (2017). Structure of a VirD4 coupling protein bound to a VirB type IV secretion machinery. EMBO J. *36*, 3080–3095.

Rohde, M., Puls, J., Buhrdorf, R., Fischer, W., and Haas, R. (2003). A novel sheathed surface organelle of the *Helicobacter pylori cag* type IV secretion system. Mol. Microbiol. *49*, 219–234.

Shaffer, C.L., Gaddy, J.A., Loh, J.T., Johnson, E.M., Hill, S., Hennig, E.E., McClain, M.S., McDonald, W.H., and Cover, T.L. (2011). *Helicobacter pylori* exploits a unique repertoire of type IV secretion system components for pilus assembly at the bacteria-host cell interface. PLoS Pathog. *7*, e1002237.

Shu, A.C., Wu, C.C., Chen, Y.Y., Peng, H.L., Chang, H.Y., and Yew, T.R. (2008). Evidence of DNA transfer through F-pilus channels during *Escherichia coli* conjugation. Langmuir *24*, 6796–6802.

Tanaka, J., Suzuki, T., Mimuro, H., and Sasakawa, C. (2003). Structural definition on the surface of *Helicobacter pylori* type IV secretion apparatus. Cell. Microbiol. *5*, 395–404.

Wallden, K., Rivera-Calzada, A., and Waksman, G. (2010). Type IV secretion systems: versatility and diversity in function. Cell. Microbiol. *12*, 1203–1212.

Cell Reports, Volume *23*

Supplemental Information

In Vivo Structures of the *Helicobacter pylori cag* Type IV Secretion System

Yi-Wei Chang, Carrie L. Shaffer, Lee A. Rettberg, Debnath Ghosal, and Grant J. Jensen

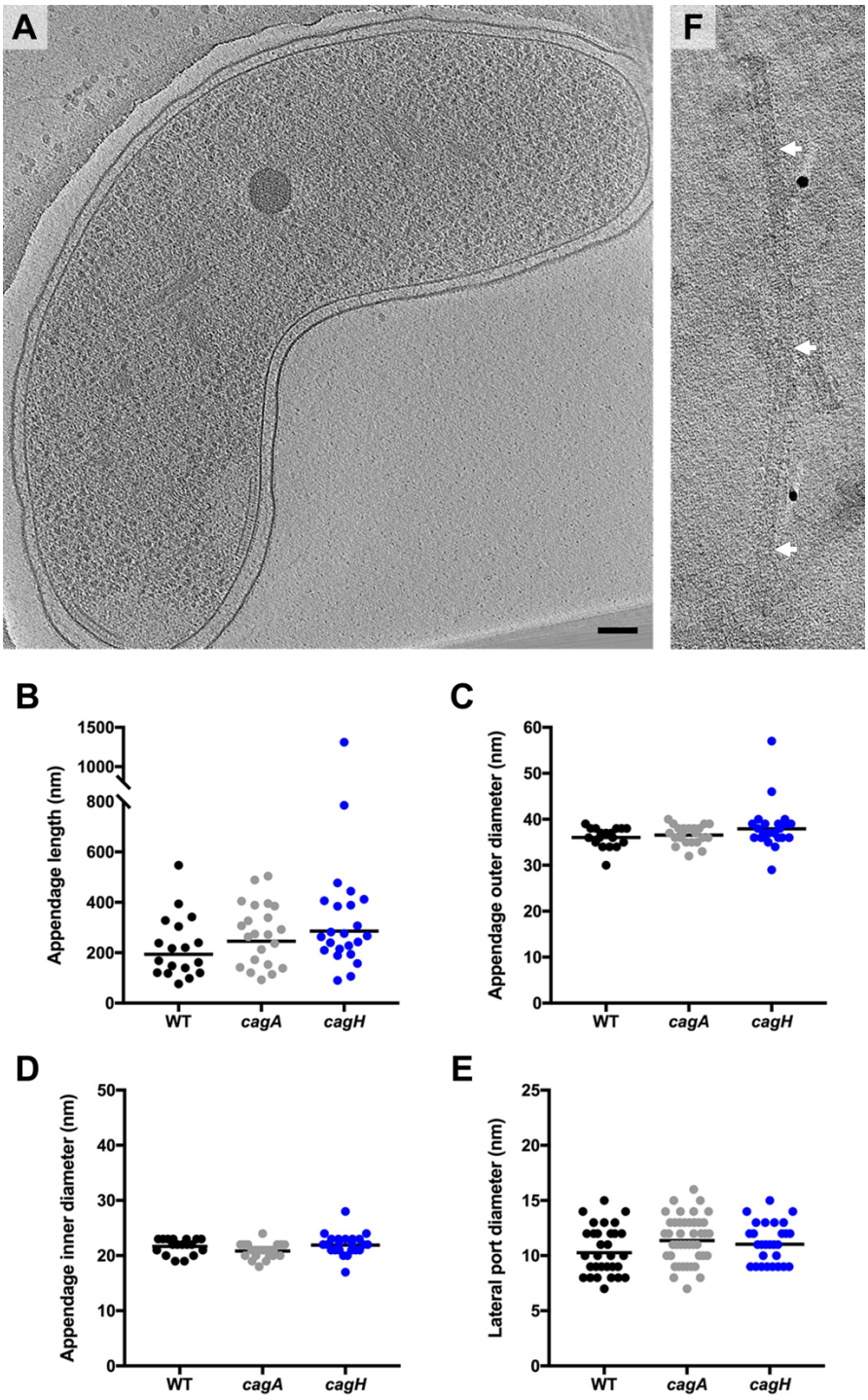

Figure S1. Tomographic features of *H. pylori* and *cag* T4SS-dependent membrane tubes, Related to Figure 1. (**A**) Tomographic slice of wild-type *H. pylori* 26695 cultured without human gastric epithelial cells. (**B-E**) Dimensions of *H. pylori* membrane tubes. (**B**) Tube length for each imaged strain. (**C**) Outer and (**D**) inner diameter of bacterial tube structures. (**E**) Width of lateral pipe-like conduits associated with some tubes. Dots in (B-D) represent the dimensions of individual tubes; dots in (E) represent the diameters of individual lateral ports. Lines represent the median of each distribution. (**F**) A tomographic slice of a >1,300 nm long tube (arrows) captured on the *H. pylori cagH* knockout strain in co-culture with human gastric epithelial cells. Smaller adjacent tubes can be seen flanking the central, long tube. Scale bar in (A) 100 nm, applies to (A) and (F).

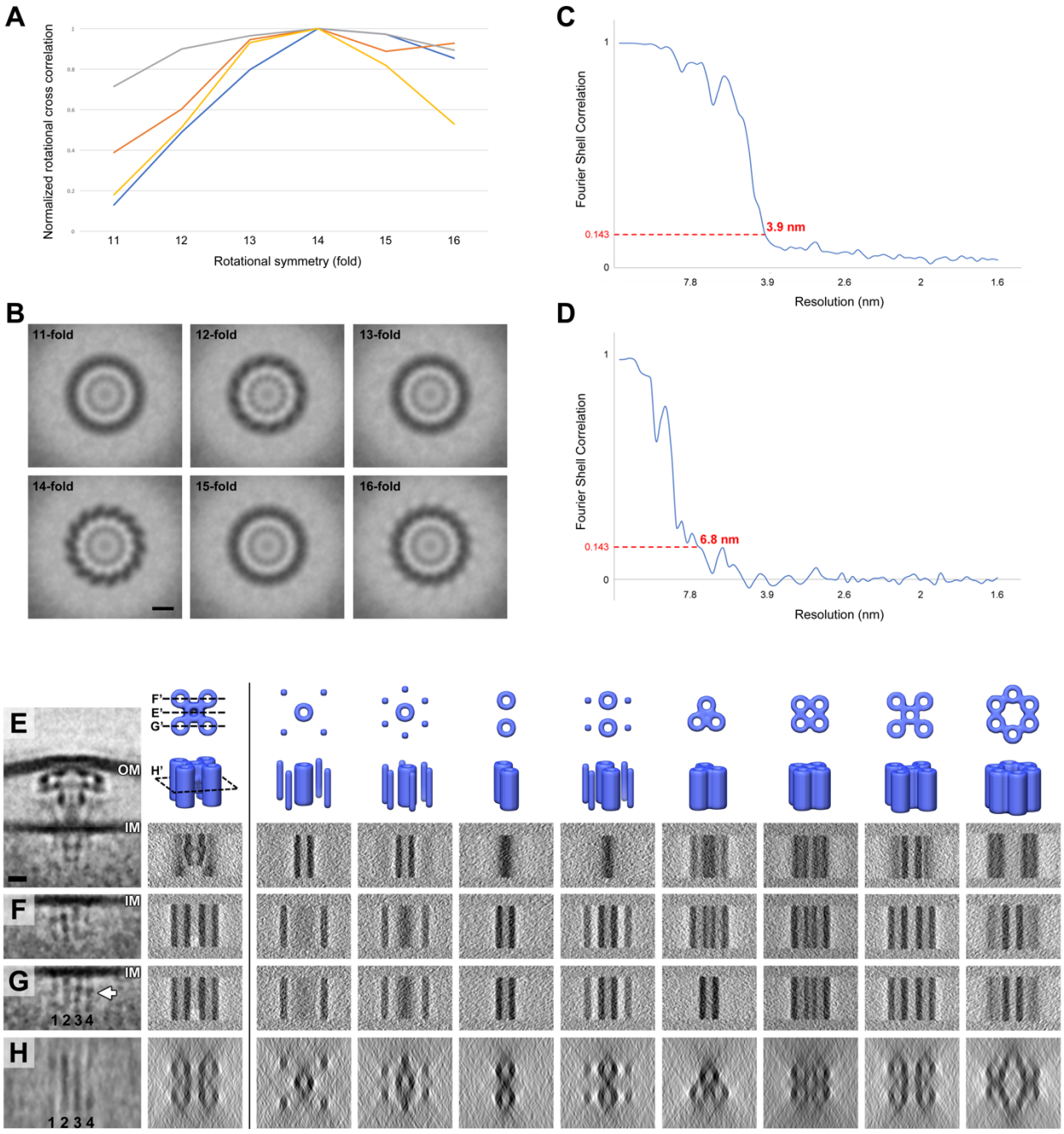

Figure S2. Modeling structures of the *cag* T4SS apparatus, Related to Figure 2. (**A** and **B**) Symmetry of the *cag* T4SS top view. (**A**) Normalized rotational cross correlation plot of four individual *cag* T4SS particles with the best top views. Each colored line indicates one particle. All of the particles show the highest score at 14-fold symmetry. (**B**) Slices through *cag* T4SS sub-tomogram averages showing the top views with 11- to 16-fold symmetrizations. The 14-fold symmetry displayed the most well-defined features of the outer ring. Scale bar in B, 10 nm. (**C**) Fourier shell correlation plot of *cag* T4SS sub-tomogram averages aligned on the periplasmic region and (**D**) the cytoplasmic region. (**E-H**) Models depicting potential structures of the *cag* T4SS cytoplasmic apparatus. (**E**) Central slice of the sub-tomogram average of the *cag* T4SS from the *en face* view. (**F**) Distal and (**G**) proximal off-center tomographic slices through the *en face* view of the *cag* T4SS particle. (**H**) Cross-section of the cytoplasmic apparatus parallel to the inner membrane at the position indicated by the white arrow in (G). From the second column onward, the top two images are the top and side views of the candidate 3D models for the cytoplasmic apparatus. The four tomographic slices below the 3D models in each column are the sections corresponding to the first column (E-H). In the second column,

E’, F’, G’ and H’ on the top two views of the 3D representation indicate the locations of the tomographic slices shown in (E-H) through the object. Comparing candidate structural models to the experimental data, we predict that the cytoplasmic apparatus is comprised of a five-barrel arrangement. Scale bar in (E) 10 nm, applies to panels (E-H). OM, outer membrane; IM, inner membrane.

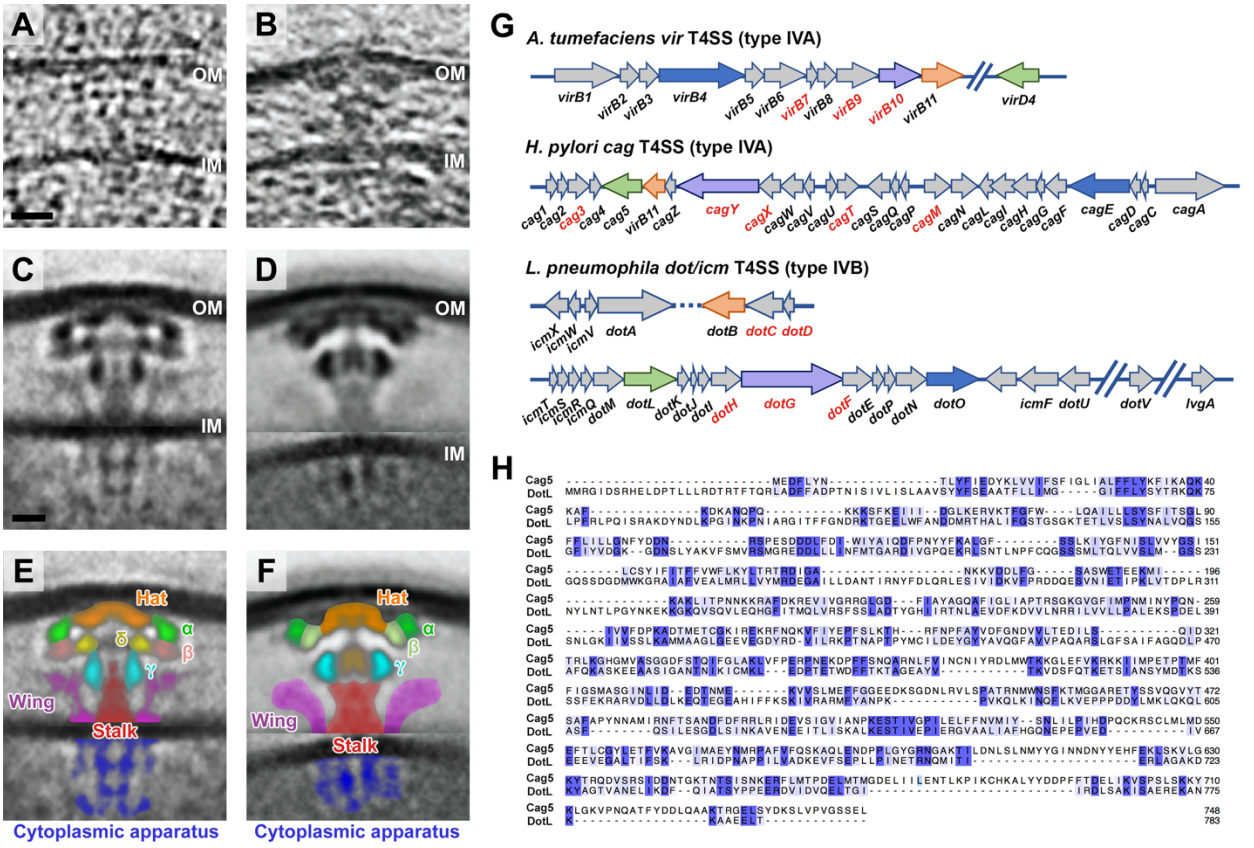

Figure S3. Schematic of structural features associated with the *cag* T4SS, Related to Figure 4. (**A**) Cryotomographic slice 7.8 nm thick through an individual *cag* T4SS particle in a tomogram of *H. pylori*. (**B**) Cryotomographic slice 7.8 nm thick through a *dot/icm* T4SS particle in a tomogram of *L. pneumophila.* (**C**) Sub-tomogram averages of the *cag* T4SS (this study) and (**D**) the *L. pneumophila dot/icm* T4SS (Ghosal et al., 2017). Composite sub-tomogram averages in C and D are aligned on the periplasmic and cytoplasmic portions of the apparatus and are stitched using the inner membrane as the boundary. (**E** and **F**) Colorized densities observed in sub-tomogram averages shown in C and D, respectively. (**G**) Genetic organization of *A. tumefaciens vir* genes, the *H. pylori cag* pathogenicity island, and *L. pneumophila dot/icm* gene regions. Colored arrows indicate recognized homologs in each T4SS. Genes encoding components of the presumed 'core complex' in each system are indicated by red text. (**H**) Protein sequence alignment of the VirD4 coupling proteins Cag5 (*H. pylori*) and DotL (*L. pneumophila*). Protein sequences were aligned using BLAST align, and aligned sequences were visualized using Jalview (Waterhouse et al., 2009). Numbers indicate the position of each residue in the pair-wise sequence alignment. Shading indicates level of sequence conservation. Scale bar in (A) 20 nm, applies to (A, B); scale bar in (C) 10 nm, applies to (C-F). OM, outer membrane; IM, inner membrane.

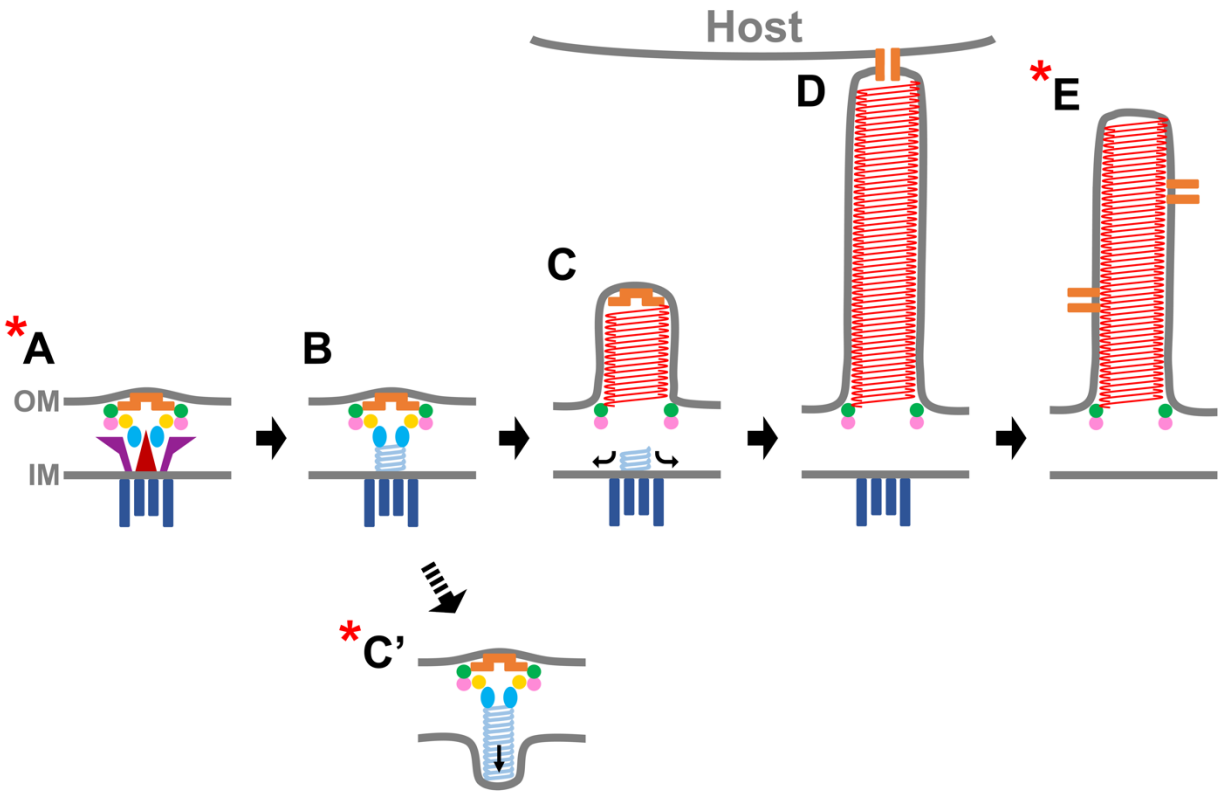

Figure S4. Working model for biogenesis of the *cag* T4SS. Related to Figure 4. See Discussion for proposed identities and roles of structures. The starred structures (A, C', and E) represent the long-lived states observed in the cryotomograms, while other stages of assembly are hypothesized.

SUPPLEMENTAL EXPERIMENTAL PROCEDURES

Sample preparation for electron cryotomography. Freshly glow discharged, UV sterilized Quantifoil gold Finder holey carbon grids (Quantifoil Micro Tools) were submerged in complete RPMI medium in 90-mm diameter cell culture dishes. AGS cells were then added to culture dishes, and cells were grown overnight at 37°C in 5% CO_2 to permit adherence to the grids. Grids were screened for cell confluency, and grids containing AGS cell clusters were inoculated with *H. pylori* at a multiplicity of infection (MOI) of approximately 50 bacterial cells per AGS cell. After infection at 37°C in 5% CO_2 (ranging from 90 min – 4.5 h), the grids were removed using forceps, loaded into an FEI Vitrobot Mark IV (Thermo Fisher Scientific) controlled at 37°C and 100% humidity, applied with 20 nm colloidal gold beads (Sigma-Aldrich) that were concentrated and pre-treated with bovine serum albumin (Iancu et al., 2006), blotted and plunge-frozen in a liquid ethane/propane mixture (Tivol et al., 2008), and stored in liquid nitrogen prior to imaging.

Electron cryotomography data collection and processing. Frozen-hydrated samples were imaged in an FEI Polara 300 keV field emission gun transmission electron microscope (Thermo Fisher Scientific) equipped with a Gatan energy filter and a Gatan K2 Summit direct detector. Energy-filtered tilt-series of images (3838 x 3710 pixels) of the cells were automatically collected from 0° to -60° and then +1° to +60° at 1° intervals using UCSF tomography data collection software (Zheng et al., 2007), with a total dosage of 160 $e^- Å^{-2}$ per tilt-series, a defocus of −6 µm and a pixel size of 3.9 Å. The images were then binned by 2 (pixel size of 7.8 Å), aligned and contrast transfer function-corrected using the IMOD software package (Kremer et al., 1996). SIRT reconstructions were subsequently produced using the TOMO3D program (Agulleiro and Fernandez, 2011) to enhance the contrast of images for better alignment in sub-tomogram averaging. The *cag* T4SS structures were located by visual inspection and extracted with a box size of 100 x 150 x 100 pixels. The sub-tomogram averages were produced using the PEET program (Nicastro et al., 2006) with local masks on either the periplasmic or cytoplasmic part. To align the periplasmic part using PEET, the rotational search ranges and steps about the axis X, Y (particle long axis perpendicular to the membranes), and Z were: (iteration 1) 6°/2°, 30°/10°, 6°/2°; (iteration 2) 3°/1°, 15°/5°, 3°/1°; (iteration 3) 1.5°/0.5°, 7.5°/2.5°, 1.5°/0.5°; (iteration 4) 0.75°/0.25°, 3.75°/1.25°, 0.75°/0.25°; (iteration 5) 0.75°/0.25°, 1.875°/0.625°, 0.75°/0.25°. To align the cytoplasmic part, the rotational search ranges and steps about the axis X, Y, and Z were: (iteration 1) 6°/2°, 180°/60°, 6°/2°; (iteration 2) 6°/2°, 90°/30°, 6°/2°; (iteration 3) 6°/2°, 45°/15°, 6°/2°; (iteration 4) 6°/2°, 22.5°/7.5°, 6°/2°; (iteration 5) 3°/1°, 11.25°/3.75°, 3°/1°; (iteration 6) 1.5°/0.5°, 5.625°/1.875°, 1.5°/0.5°; (iteration 7) 0.75°/0.25°, 2.8125°/0.9375°, 0.75°/0.25°; (iteration 8) 0.75°/0.25°, 1.40625°/0.46875°, 0.75°/0.25°. A 14-fold symmetry and a 2-fold symmetry were applied to the periplasmic and cytoplasmic parts, respectively, for the final results. The Fourier shell correlation plots shown in Figure S2 were generated using PEET. The surface rendering in Figure 2 was generated using the UCSF Chimera program (Pettersen et al., 2004).

SUPPLEMENTAL REFERENCES

Agulleiro, J.I., and Fernandez, J.J. (2011). Fast tomographic reconstruction on multicore computers. Bioinformatics *27*, 582-583.

Iancu, C.V., Tivol, W.F., Schooler, J.B., Dias, D.P., Henderson, G.P., Murphy, G.E., Wright, E.R., Li, Z., Yu, Z., Briegel, A.*, et al.* (2006). Electron cryotomography sample preparation using the Vitrobot. Nat Protoc *1*, 2813-2819.

Kremer, J.R., Mastronarde, D.N., and McIntosh, J.R. (1996). Computer visualization of three-dimensional image data using IMOD. J Struct Biol *116*, 71-76.

Nicastro, D., Schwartz, C., Pierson, J., Gaudette, R., Porter, M.E., and McIntosh, J.R. (2006). The molecular architecture of axonemes revealed by cryoelectron tomography. Science *313*, 944-948.

Pettersen, E.F., Goddard, T.D., Huang, C.C., Couch, G.S., Greenblatt, D.M., Meng, E.C., and Ferrin, T.E. (2004). UCSF Chimera--a visualization system for exploratory research and analysis. J Comput Chem *25*, 1605-1612.

Tivol, W.F., Briegel, A., and Jensen, G.J. (2008). An improved cryogen for plunge freezing. Microsc Microanal *14*, 375-379.

Waterhouse, A.M., Procter, J.B., Martin, D.M., Clamp, M., and Barton, G.J. (2009). Jalview Version 2--a multiple sequence alignment editor and analysis workbench. Bioinformatics *25*, 1189-1191.

Zheng, S.Q., Keszthelyi, B., Branlund, E., Lyle, J.M., Braunfeld, M.B., Sedat, J.W., and Agard, D.A. (2007). UCSF tomography: an integrated software suite for real-time electron microscopic tomographic data collection, alignment, and reconstruction. J Struct Biol *157*, 138-147.